Journal of Electroceramics 3:2, 151–162, 1999
© 1999 Kluwer Academic Publishers, Boston. Manufactured in The Netherlands.

Optimized PZT Thin Films for Pyroelectric IR Detector Arrays

RAINER BRUCHHAUS, DANA PITZER, MATTHIAS SCHREITER & WOLFRAM WERSING
Siemens AG, Corporate Technology, ZT MF 2, D-81730 Munich, Germany

Abstract. A planar multi target sputtering technology was used to deposit highly (111) oriented $Pb(Zr_xTi_{1-x})O_3$ (PZT) thin films with x ranging from 0–0.6. The preparation of a stable Pt/ZrO_2 electrode is described and analyzed in terms of stress and stress-temperature behavior. The PZT films with low Zr content are under compressive stress after deposition. The dielectric constant and loss peaks occur at a composition close to the morphotropic phase boundary. Films on the tetragonal side of the phase diagram with a Zr content up to about 25% exhibited a strong self polarization and strong voltage shifts in the C(V) curves. High pyroelectric coefficients of $> 2 \times 10^{-4}$ C/(m^2K) have been measured on these films without additional poling. The self polarization fades out with increasing Zr content. The low values of the pyroelectric coefficient for the PZT film with 60% Zr is discussed in terms of the possible crystallographic variants after distortion and the tensile stress state during the phase transition. Based on the systematic study of stress and electrical properties of PZT films with a wide range of composition presented in this paper, films with a Zr content up to about 25% turned out to give the best properties for the use in pyroelectric detector arrays.

Keywords: PZT thin films, PZT composition, multi target sputtering, stress, electrical properties, self-polarization

1. Introduction

Recently, ferroelectric thin films have received a great deal of attention in the integration of these films with Si integrated circuits for a variety of applications. The remanent polarization of these materials is used for non-volatile data storage in so called ferroelectric RAMs. The pyroelectric effect is utilized in thin film pyroelectric IR detector arrays for the thermal detection of objects and persons. Lead oxide based perovskites such as $PbTiO_3$, $Pb(Zr,Ti)O_3$ (PZT) and $(Pb,La)(Zr,Ti)O_3$ (PLZT) are preferred for this application because of their high pyroelectric coefficient, low dielectric loss, high resistivity and high Curie temperature.

Pyroelectric IR detectors are uncooled thermal sensors in which long wavelength IR radiation is converted into a temperature change. This change is detected by the release of charge on a parallel plate capacitor structure due to the pyroelectric effect. One key to achieve high detectivity is to reduce the heat capacity of the pyroelectric element and the heat conduction into the substrate. Therefore, the sensing elements are arranged on thin micromachined membranes as a mechanical support structure [1–4]. For reliable sensors as well as high yield in the fabrication of these devices the mechanical properties of the membrane as well as of the electrode layers and the ferroelectric film are as important as the electrical performance of the pyroelectric capacitor. Moreover, in ferroelectrics the electrical properties are directly related to the mechanical stress state of the film. Tuttle et al. [5] used substrates with different thermal expansion coefficients to prepare rhombohedrally distorted PZT (60/40) films. They found vastly different electrical properties when deposited on Si substrates or sapphire substrates covered with an thin Pt electrode. In the mentioned paper it is demonstrated that the 90° domain orientation in the ferroelectric PZT films is largely controlled by the stress at the transformation temperature. It is evident that the understanding of mechanical stress during processing

of the different layers on the Si substrate is necessary for the optimization of thin film pyroelectric IR detector arrays.

The influence of stresses in $BaTiO_3$ thin films on the properties have been discussed in detail by Desu [6]. Stress evolution of electrode materials and PZT (52/48) during processing have been described by Spierings et al. [7,8] and by Sengupta et al. for $PbTiO_3$ [9]. It is demonstrated that the electrodes are in a tensile stress state after crystallization of the ferroelectric and that the switching behavior of the PZT capacitors is directly related to the stress state of the ferroelectric film. The same group describes in another paper stresses in $Ru/PbZr_{0.4}Ti_{0.6}O_3/Ru$ thin film stacks [10]. The PZT film is prepared by MO CVD at a substrate temperature of 725°C. In contrary to the films prepared by the sol-gel method the MOCVD ferroelectric film is under considerable compressive stress after deposition. XRD methods have been used to analyze the mechanical properties of Nd-modified PZT(55/45) films on MgO and Si substrates prepared by laser ablation [11]. For the film on MgO a compressive stress of – 226 MPa was found. The film on the Si substrate exhibited a tensile stress of 415 MPa. This is due to the difference in thermal expansion coefficients of the substrate and the film. MgO has a higher coefficient than the PZT film and the expansion coefficient of Si is smaller resulting in the different stress states after cooling from the crystallization temperature at which the film is expected to be nearly stress free. Electrode stresses and stresses of sputter deposited tetragonal PZT films are described in two recent papers [12,13]. The ferroelectric phase transition is observed in stress-temperature plots due to the changes in expansion coefficients close to the Curie point of the ferroelectric layer. The stress levels of the ferroelectric film after cooling from the deposition temperature are low for the sputter deposited films making them useful for the mechanical membrane structure in the integrated pyroelectric detector arrays.

In the present paper a systematic study about stresses in sputter deposited thin films with compositions ranging from 0% to 60% Zr together with stress temperature plots of these films is presented. In addition, electrical results on patterned test capacitors are given. It will be demonstrated that the composition dependent stress state of the film directly affects the electrical properties.

2. Device Design and Processing

In a thin film pyroelectric IR detector array the incoming IR radiation is transformed into a temperature change within the pyroelectric pixel. To achieve sensors with high detectivity the mechanical structure must be optimized in terms of low heat capacity and low thermal conduction into the substrate. Extensive thermal modeling was used to define the mechanical structure of an 11×6 pyroelectric detector array. Figure 1 gives a SEM micrograph of a part of the array. The pyroelectric pixels are arranged on an about 1 μm thick SiO_2/Si_3N_4 membrane. The pixels have a sensitive area of $280 \times 280\,\mu m^2$, a column pitch of 500 μm and a row pitch of 660 μm. All pixels have a common back electrode. 64 top electrodes are separately connected to bonding pads via metallization lines, two pixels are not connected to the read-out circuit. Between the pixels metal stripes are arranged as a heat sink to suppress cross-talking between the pixels in one column. The pyroelectric chip is connected to the read-out circuit by wire bonding. The read-out circuit (not shown in Fig. 1) is fabricated in a 2 μm CMOS-technology. For every pixel an input circuit module consisting of a charge-voltage converter and a bandwidth limiting RC low-pass filter is existing. The signals of the 64 input modules are time multiplex connected to the output amplifier.

Figure 2 gives a flow chart of the pyroelectric pixel processing using bulk micromachining. As a substrate

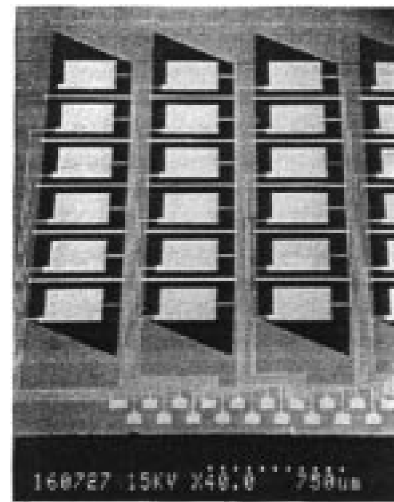

Fig. 1. SEM micrograph of the detector array structure using bulk micromachining for defining the mechanical structure.

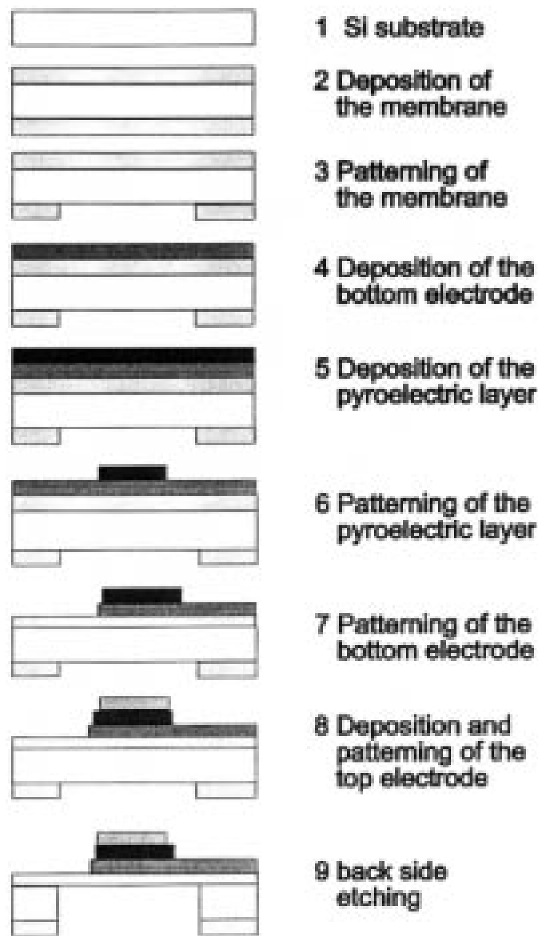

Fig. 2. Flow chart of pyroelectric pixel processing.

a 4'' (110) oriented double side polished Si wafer is used. In the first deposition step an about 1 μm thick SiO_2/Si_3N_4 membrane is deposited on both sides of the wafer. After that the membrane is patterned on the back side of the wafer (step 3). The Pt bottom electrode and the pyroelectric PZT film are deposited on the membrane layer on the front side of the wafer (steps 4 and 5). In the 6th processing step the pyroelectric layer is patterned by wet chemical etching. For the patterning of the bottom electrode in the 7th processing step ion beam etching is used. The top CrNi electrode is deposited and patterned by a lift off process (step 8). The last processing step includes the back side etching of the silicon underneath the pyroelectric capacitor by anisotropic KOH etching. In this 9th processing step the membrane layers serve as a mask as well as an etch stop underneath the bottom electrode. More processing steps not shown in Fig. 2 include the deposition of the metallization lines by a lift off process. These lines together with the bonding pads are seen in the SEM micrograph of the array, Fig. 1.

3. Experimental

PZT thin films with a composition ranging from 0% Zr to 60% Zr have been prepared by multi-target sputtering. Details of the sputtering system are given in [12]. In summary, films are prepared by planar reactive sputtering from three metallic targets. The advantage of that sputtering approach is the ease of stoichiometry variation of the ferroelectric film. Simply by changing the electrical power to the target the flux of the material from the target to the substrate can be adjusted [14–16]. The films are deposited ''in-situ'' on preheated substrates. The substrate temperature for the films prepared for this paper was about 580°C. Table 1 gives the sputtering conditions.

PZT film thickness ranged from 700 nm to 1200 nm. The PZT was deposited on thermally oxidized 4″ Si-wafers with an oxide thickness of 500 nm covered with a thin Pt electrode. Oxidic ''glue'' layers were used to promote Pt adherence to the underlying thermal oxide [17]. The electrodes were deposited in a Perkin Elmer 2400 RF sputtering system equiped with 8″ targets. During deposition the substrates were heated to temperatures ranging from 250°C up to 560°C.

Crystalline phases and orientation have been analyzed by standard θ-2θ X-ray diffraction (XRD). The composition of the ferroelectric films was

Table 1. Sputtering conditions of the PZT films with different composition. Sputtering pressure is 1.4 Pa, substrate temperature is 580°C, sputtering gas composition is 50% Ar/50% O_2, table rotation 10 rpm

Sample	Power Pb 91$^-$ target [W]	Power Ti-target [W]	Power Zr-target [W]
PZT(0/100)	190	2900	0
PZT(10/90)	210	2900	56
PZT(20/80)	255	2900	156
PZT(24/76)	290	2850	400
PZT(38/62)	450	2800	700
PZT(44/56)	470	2850	885
PZT(48/52)	510	2300	934
PZT(60/40)	540	1350	832

analyzed by electron microprobe micro analysis (EPMA) with a PZT ceramics sample used as a standard.

The thin film stresses were analyzed by measuring the wafer warpage before and after film deposition using a Tencor FLX 2900 stress analyzer. In addition, this instrument is capable to measure the bow of the wafer as a function of temperature up to 900°C for the analysis of thermal stress. For the experiments described in this paper the heating rate for the wafers was 10 K/min and the soak time at maximum temperature was 10 min. The cooling rates were 3–6 K/min, all experiments have been performed in ambient air.

For electrical characterization the films were patterned to test capacitors using a three mask photolithographic process. In the first step a Pt top electrode of 100 nm thickness was patterned by a lift off process. In the second step the PZT film was etched by wet chemical etching using a photoresist mask. In the third step the bottom Pt electrode was etched by ion beam etching. Test capacitor area ranged from $50 \times 50\,\mu m^2$ to $800 \times 800\,\mu m^2$. The design of the test capacitors is given in [16]. The pyroelectric coefficient was measured by periodically heating and cooling (thermochuck from ERS company, type wafertherm SP 73 A) the sample and measuring the current with a sensitive electrometer (Keithley 6517). The ''HIGH'' input of the electrometer is connected to the bottom electrode. The capacity and dielectric loss of the test capacitors was measured with a HP 4275 LCR bridge at 10 kHz, test signal level was 0.1 V. For the analysis of the switching behavior of the ferroelectric films, slow ramp C(V) curve measurements were performed. To estimate the degree of self polarization additional poling of the test capacitors was performed at 100°C with a poling voltage of 20 V/μm for 5 min and the electric field in the direction of the self polarization.

4. Results and Discussion

4.1. Stress Evolution during Processing of Pt Electrodes with ZrO_2 *Adherence Layer*

ZrO_2 films are deposited from a ZrO_2-target by rf sputtering at a pressure of 0.67 Pa and a substrate temperature of 440°C. The films exhibit a featureless surface in the SEM, Fig. 3.

The 50 nm thick film is under high compressive stress of -1950 MPa. The film was thermally cycled in the stress analyzer to a temperature of 600°C, Fig. 4.

Up to a temperature of 400°C which is close to the deposition temperature the compressive stress increases. This is due to the higher thermal expansion coefficient of ZrO_2 (cubic ZrO_2: $\alpha = 7.5$–$13 \times 10^{-6}\,K^{-1}$ [19]) compared to the silicon substrate. Above 400°C stress relief of the ZrO_2 film sets in. After the 10 min soak time at 600°C the stress

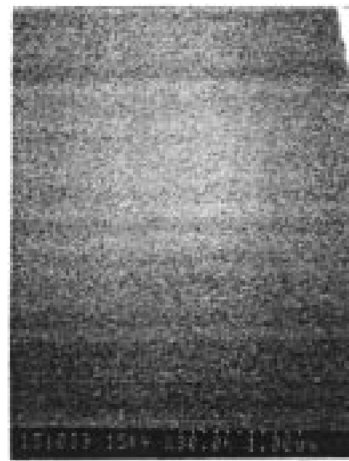

Fig. 3. SEM of the surface of a sputter deposited ZrO_2 film exhibiting a featureless surface structure.

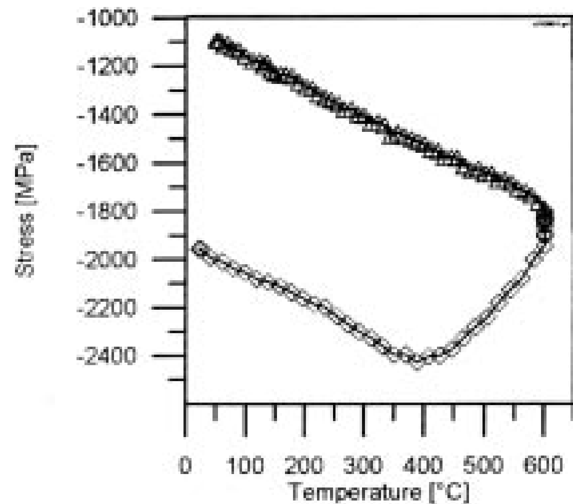

Fig. 4. Stress-temperature plot of a ZrO_2 film, 1st cycle thermal cycle to 600°C. (◇ heating, △ cooling).

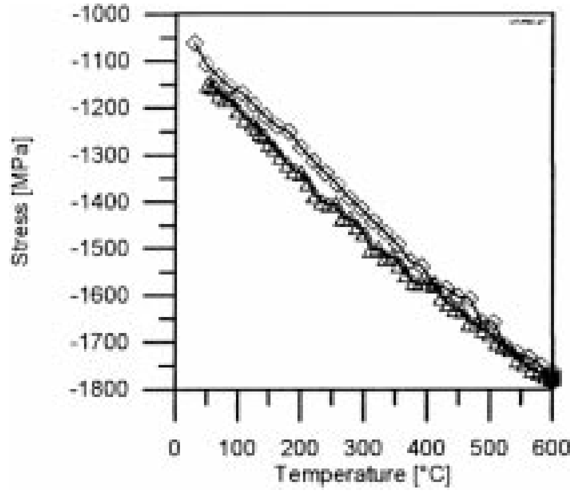

Fig. 5. Stress-temperature plot of a ZrO_2 film, 2nd thermal cycle to 600°C (◇ heating, △ cooling).

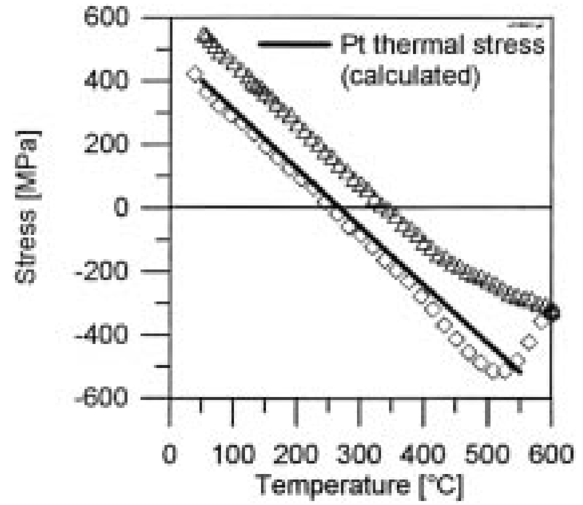

Fig. 6. Stress-temperature plot of a ZrO_2/Pt electrode, 1st thermal cycle to 600°C. (◇ heating, △ cooling, — calculated thermal stress of Pt).

is still on a high level of − 1800 MPa, i.e., even at 600°C only part of the intrinsic stress from the sputtering process is relaxed.

During cooling the compressive stress decreases linearly indicating an elastic behavior of the oxide. After the thermal cycle the stress has been reduced to − 1100 MPa. In a second thermal cycle up to 600°C the heating and cooling curves overlapp indicating a stabilized stress temperature behavior after the first thermal cycle, Fig. 5.

The stress of the 20 nm ZrO_2/60 nm Pt electrode depends on the substrate temperature during deposition, Table 2.

Compared to the high compressive stress of the ZrO_2 adhesion layer deposited at 440°C the ZrO_2/Pt electrode is under tension after deposition. The compressive stress of the ZrO_2 layer is counterbalanced by a tensile stress of the top Pt layer. The substrate temperature as well as the thickness ratio ZrO_2/Pt can be used to taylor the stress of the electrode. A 8 nm ZrO_2/60 nm Pt film deposited at 400°C has a tensile stress of 420 MPa according to the

Table 2. Stress of 20 nm ZrO_2/60 nm Pt electrodes deposited at substrate temperatures ranging from 250 to 560°C

Substrate temperature [°C]	Stress [MPa]
250	− 140
440	80
560	200

higher Pt/ZrO_2 thickness ratio. On the other hand, decreasing the temperature to 250°C gives an overall compressive stress. A 20 nm ZrO_2/60 nm Pt electrode deposited at 560°C exhibited a tensile stress of 200 MPa.

Figure 6 gives the first thermal cycle up to 600°C of the 8 nm ZrO_2/60 nm Pt electrode stack. At a temperature of 250°C the stress becomes compressive and up to 500°C an elastic behavior indicated by the linear slope is found. Above 500°C a stress relief of about 200 MPa is found.

On cooling the ''zero'' stress temperature has increased to 350°C and the room temperature stress to 550 MPa. It is expected that the Pt metal film grows in a stress free state at 440°C. During cooling a tensile stress develops due to the higher thermal expansion coefficient of the Pt compared to the silicon substrate. Equation (1) gives the thermal stress which originates from different thermal expansion coefficients of the substrate (α_s) and the film (α_f) over a temperature difference from a higher T_{anneal} to a lower T_0 (room temperature). E_f is the Young's modulus of the film, ν_f the Poisson ratio.

$$\sigma_{th} = \frac{E_f}{1-\nu_f} \int_{T_{anneal}}^{T_0} (\alpha_f - \alpha_s) dT \qquad (1)$$

For the calculated stress in Fig. 6 $\alpha_s = 2.8 \times 10^6 K^{-1}$ for the Si substrate, $\alpha_f = 9.4 \times 10^{-6} K^{-1}$ for the

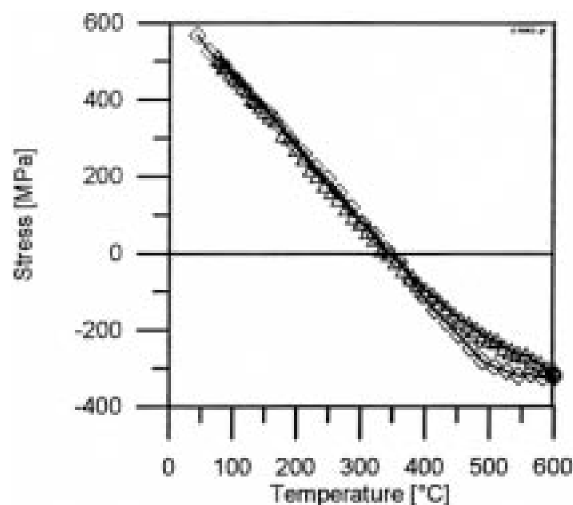

Fig. 7. Stress-temperature plot of a ZrO_2/Pt electrode, 2nd thermal cycle to 600°C. (◇ heating, △ cooling).

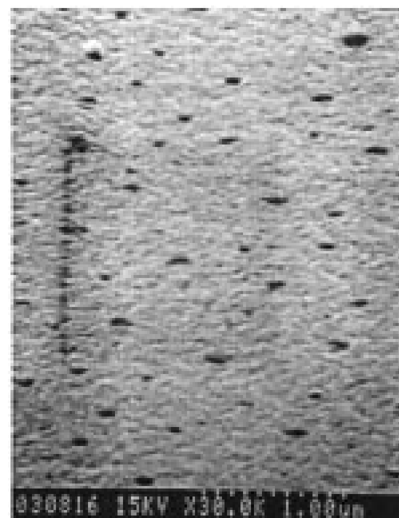

Fig. 8. SEM micrograph of the surface structure of a ZrO_2/Pt electrode after 2nd annealing in air to 600°C exhibiting small hillocks.

Pt film [18], $E_f = 170$ GPa and $\nu_f = 0.39$ [7] have been used for the calculation. The measured and calculated curves nicely fit together indicating that mainly the thermal stress of the nearly eight times thicker Pt film is measured.

Figure 7 gives the second thermal cycle of the ZrO_2/Pt electrode of Fig. 4. Same as for the ZrO_2 film, the heating and cooling curve overlap over a wide temperature range, i.e., the stress relief of the Pt film was nearly complete after the first thermal cycle.

The stress temperature curve of the first thermal cycle found for the sputtered ZrO_2/Pt electrode is very similiar to that found for electron beam evaporated films [20]. In that paper the ZrO_2 film was formed by complete oxidation of a 20 nm Zr metal film at 1 Torr oxygen at 330°C for 5 min and 425°C for 20 min. This procedure is similiar to that described for TiO_2/Pt electrodes [12] for which a thin Ti metal film is transformed to TiO_2 by RTP annealing in flowing oxygen gas. On top of the so formed ZrO_2 a Pt film is deposited by evaporation. This electrode is subjected to annealing at different temperatures and simultaneously the wafer bow is measured. At temperatures of about 500°C the electrode is under high compression and a stress relief is found. During stress relief Pt hillocks are formed found by AFM analysis of the surface [20]. The driving force for the hillock formation is the relaxation of film stress. Small hillocks are also found on the sputtered ZrO_2/Pt electrode subjected to two anneals in air up to 600°C. Figure 8 gives a SEM micrograph of the surface structure.

4.2. Multi-Target Sputtering Process for PZT

The PZT films for this investigation have been deposited at a substrate temperature of about 580°C in a so called ''one-step'' process, i.e., the substrate temperature is sufficiently high to grow the film in the perovskite phase without the need of a further crystallization step. In the PZT solid solution system the phase transformation temperature decreases with increasing Zr content. For pure $PbTiO_3$ ceramics a Curie point of about 490°C is reported [21], ceramics with $Zr/(Zr + Ti) = 0.6$ have a Curie point of about 360°C. Therefore, the sputter deposited films are expected to be grown in the cubic phase. The phase transformation either cubic to tetragonal for the Ti rich compositions or cubic to rhombohedral for the Zr rich compositions will be performed during the cooling process after the targets and the substrate heater have been switched off.

A reactive sputtering approach depositing the material from metallic targets has been used. One advantage compared to the deposition from ceramic PZT targets is that usually the metals are available with a higher purity and due to the higher heat

conduction of the metals the targets can be used at a higher power density. The power at the Ti target for the Ti rich compositions was 2900 W, i.e., a power density of 8.9 W/cm^2. The advantage of the multi target deposition is the ease to vary the stoichiometry of the films simply by changing the power to the targets. In Table 1 detailed conditions are given. Another challenge in the deposition of lead oxide containing ferroelectric materials is the possible lead loss at elevated substrate temperatures. With the multi target sputtering this possible lead loss in the film can be easily compensated by a higher power to the Pb target. Maeder et al. [22] have investigated the ratio between the sputtered flux and the amount of lead which is incorporated in the film. In addition, the amount of incorporated lead depends on the Zr/Ti ratio of the deposited film. From Table 1 the power ratio $P_{Pb}/(P_{Zr} + P_{Ti})$ needed to deposit a film in the perovskite phase can be calculated. For the PZT(10/90) film this ratio is 0.071 and increases with increasing Zr to 0.247 for the PZT(60/40) film, i.e., the volatility of PbO is higher in the Zr rich compositions.

The sputtering pressure and the gas composition have been chosen as 1.4 Pa and 50% oxygen in Ar. The deposition rate of a metal target strongly depends on the partial pressure of oxygen in the deposition chamber. When the oxygen partial pressure in the chamber is high, the target surface will be oxidized and the deposition rate will drop. The effect of oxygen partial pressure for the deposition of $PbTiO_3$ and $(Pb,La)TiO_3$ films has been investigated in detail by Adachi et al. [23].

The table rotation was fixed to 10 rpm. For the Ti rich compositions the deposition rate is in the range of 5–7 nm/min. For the films with a composition close to the morphotropic phase boundary the highest overall power to the targets could be supplied. These films are deposited with a rate of about 10 nm/min, thus increasing the film thickness by roughly 2 lattice constants per revolution of the substrate holder.

4.3. Texture and Morphology of the PZT Films

The PZT films grow with a prefered (111) texture. However, the film with $Zr/(Zr + Ti) = 0.60$ exhibited some minor amount of grains with (100), (110) and (112) orientation, Fig. 9.

In a very recent paper it was shown by Muralt et al. [24] that very thin textured titania seed layers almost inevitably led to (111) texture. It turned out that an optimum film thickness of TiO_2 of only between 1 and 2 nm is sufficient to obtain the (111) texture.

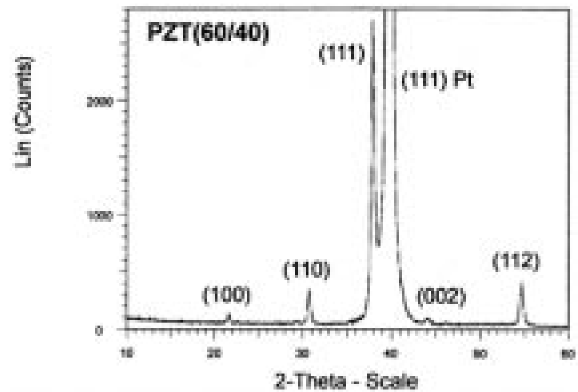

Fig. 9. XRD trace of a PZT(60/40) film.

Figure 10 gives a SEM micrograph of the surface structure of the PZT(38/62) film, micrographs of sputter deposited films with other compositions have been published in [25].

The film exhibits a homogeneous structure and consists of densely packed columnar grains with a grain size of about 200 nm.

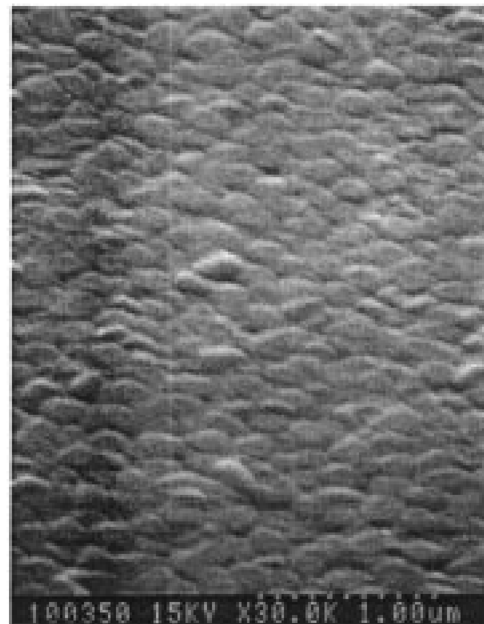

Fig. 10. SEM micrograph of the surface morphology of a PZT(38/62) film.

4.4. Stresses and Stress Temperature Behavior

The stress of the electrode/PZT stack is measured by the change of the wafer bow after each film deposition step. The total stress σ can be calculated from the difference in the radii of curvature before (R_0) and after (R) the deposition step using the Stoney formula [26], Eq. (2).

$$\sigma = \frac{E_s}{6(1-\nu_s)} \frac{{t_s}^2}{t_f} \left(\frac{1}{R} - \frac{1}{R_0} \right) \tag{2}$$

where t_f is the film thickness and E_s, ν_s and t_s are the elastic modulus, Poisson ratio and thickness of the substrate. The only film property needed to calculate the film stress is the thickness. By definition, negative values for the stress indicate a compressive and positive values a tensile stress in the film. The stress state measured after the PZT deposition is a combination of the PZT stress itself, the stress of the electrode and possible influences to the previously deposited films during the PZT process. However, as the PZT thin film is at least about eight times thicker than the underlying electrode, the radius of curvature is mainly due to the bow of the thick ferroelectric layer.

The stress state of the electrode/PZT stack after deposition strongly depends on the composition of the PZT layer. Films with low Ti content exhibit a compressive stress after deposition, films with high Zr content are under tension. To study the stress temperature behavior of the PZT film the wafers were heated in the furnace of the stress analyzer in air to 600–650°C. During the first thermal cycle relaxation of some incorporated intrinsic stress occurs [12]. To receive reversible stress temperature curves the thermal cycle was measured twice. Figure 11 gives the stress temperature curves of PZT thin films with different composition during the second cooling cycle.

As mentioned earlier the PZT films with low Zr content are under compressive stress at room temperature. The PZT(60/40) film with a composition on the rhombohedral side of the phase diagram exhibits the highest tensile stress. All curves exhibit a maximum at a certain temperature. This temperature decreases with increasing Zr content. As discussed in detail in [13] this maximum can be attributed to the Curie point of the PZT film. To some extent the stress level at room temperature is directly related to the Curie point. As indicated by the slope of the curve above the Curie point the thermal expansion coefficient of cubic phase is higher than the thermal expansion coefficient of the substrate, i.e., during cooling the tensile stress will increase down to the Curie temperature resulting in higher tensile stress levels for films with lower Curie point. The part of the curve below the Curie point with an inversed slope is directly related to the distortion. The higher the distortion the more the stress will decrease [13]. It is worth to note that at the phase transformation all the films are under tension.

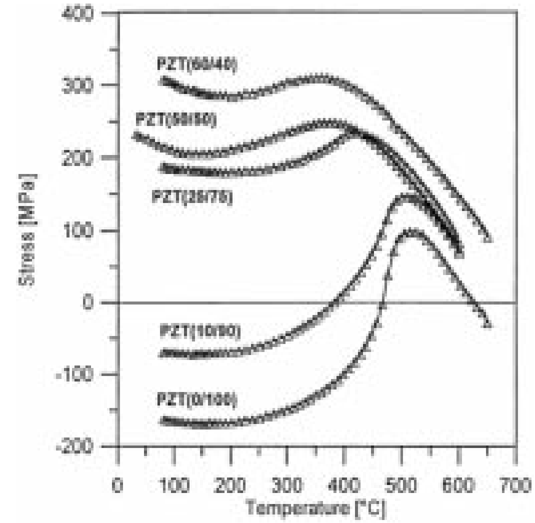

Fig. 11. Stress temperature plots of PZT thin films with Zr/(Zr + Ti) ranging from 0 to 0.6.

4.5. Electrical Characterization of the PZT Films

The sputter deposited PZT films were electrically characterized in terms of permittivity and loss, pyroelectric coefficient and slow ramp C(V) curves to study the switching behavior and the degree of internal voltage shifts. Table 3 gives an overview.

The dielectric constant increases with Zr/Ti ratio up to a composition close to the morphotropic phase boundary. On the rhombohedral side of the phase diagram the dielectric constant decreases. This expected result is in agreement with bulk ceramics as well as with PZT thin films prepared by sol gel processing and MO CVD [27,28]. The dielectric loss tan δ measured at 10 kHz increased with increasing Zr content. Up to $Zr/(Zr+Ti)=0.24$ very low values down to 0.006 have been found. The dielectric loss in

Table 3. Electrical properties of PZT thin films with different Zr/(Zr + Ti) ratio

Sample	ε_{rel}	$\tan\delta$	p[10^{-4} C/m^{2}K]	p after poling
PZT(10/90)	172	0.006	2.09	2.02
PZT(20/80)	209	0.007	2.14	2.16
PZT(24/76)	245	0.006	2.12	2.31
PZT(38/62)	539	0.01	1.57	2.5
PZT(44/56)	665	0.014	1.28	2.39
PZT(48/52)	767	0.014	0.33	1.33
PZT(60/40)	598	0.011	0.11	1.24

ferroelectric materials strongly correlates with the freedom of domain wall movement. Normally, it peaks a few degrees below the Curie point and falls to very low values as the domains disappear. For the PZT films with a Zr content up to about 25% high offset voltages are found which strongly stabilize the polarization in one direction (see discussion below). In these films domain wall movement is reduced resulting in a low dielectric loss well below 1%. With increasing Zr content the voltage offset disappears and thus the stabilizing effect. It is expected that the domain wall movement is enhanced in the films with these compositions. The dielectric loss increases by a factor of two for films with a composition close to the morphotropic phase boundary.

Films up to the composition PZT(24/76) exhibit high pyroelectric coefficients p in the as deposited state, i. e. these films are highly self polarized. Values $p > 2 \times 10^{-4}$C/(m^{2}K) are found. The sign of the electric current flowing in the heating and cooling period of the p measurement can be used to determine the direction of the prepoled state. As during the heating of the sample a positive current is measured flowing from the bottom to the top electrode it is concluded that the polarization is directed from the bottom to the top electrode. This direction has also been found in earlier publications [29,30]. The degree of self polarization decreases with increasing Zr content. Films with composition at the morphotropic phase boundary have only low values for the pyroelectric coefficient. The PZT(60/40) is not self-polarized, Fig. 12.

Figure 12 also includes the pyroelectric coefficient of films which were electrically poled after the first measurement of the pyroelectric coefficient. The poling was performed in the direction of the prepolarized state at 100°C and a poling field of 20 V/μm. The pyroelectric coefficient can not be

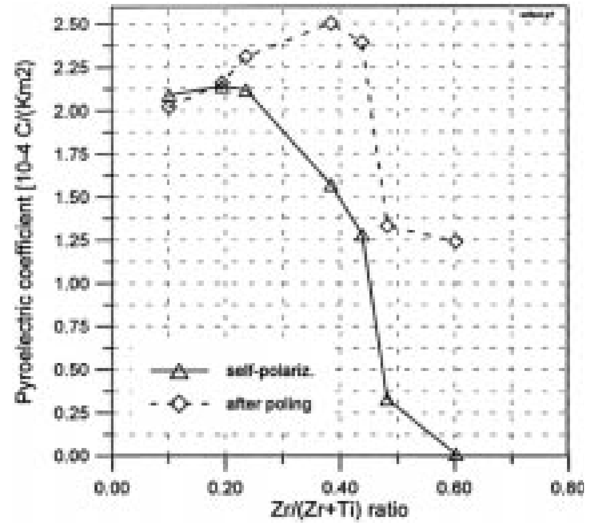

Fig. 12. Pyroelectric coefficient of PZT thin films with different Zr/(Zr + Ti) ratio in the as-deposited and poled state.

increased by the additional poling procedure for films with a composition up to Zr/(Zr + Ti) = 0.2. In the compositional range Zr/(Zr + Ti) = 0.2–0.4 the pyroelectric coefficient can be improved up to 2.5×10^{-4} C/(m^{2}K) for Zr/(Zr + Ti) = 0.4. For the composition close to the morphotropic phase boundary and on the rhombohedral side of the phase diagram the pyroelectric coefficient drops by a factor of 2 compared to the value achieved for Zr/(Zr + Ti) = 0.4.

Additional information about the degree of self-polarization and the switching behavior of the films can be received by the measurement of slow ramp C(V) curves. During the measurement the film was first biased in the direction of the prepolarized state, i.e., the measurement starts with a positive voltage sweep on the bottom electrode. After biasing the capacitor with negative voltage the measurement is continued to the maximum positive voltage and then stopped leaving the capacitor in a poled state. As an example for a highly self-polarized film, the C(V) curve of the sample with Zr/(Zr + Ti) = 0.2 is given, Fig. 13.

In the direction of the prepolarized state, i.e., with positive electric field, the curve is flat indicating that there is no polarization that can be switched. With negative electric field up to about -20 V/μm nearly no switching of the polarization can be detected. This is an indication for a very high offset voltage found in

the film which stabilizes the polarization in the direction of the prepolarized state.

In the film with Zr/(Zr + Ti) = 0.38, Fig. 14, an increased amount of switchable polarization is found during first biasing with positive electric field. At $-10\,V/\mu m$ a broad maximum in the C(V) curve is found indicating that the polarization can be switched at considerably lower electric field than the film with Zr/(Zr + Ti) = 0.2. The maximum at $2.5\,V/\mu m$ indicates the backswitching of the polarization into the ''up'' state. Compared to the film with Zr/(Zr + Ti) = 0.2 the offset voltage has reduced. The film with Zr/(Zr + Ti) = 0.6 exhibits a nearly symmetric C(V) curve, Fig. 15. A high portion of polarization switching is found during first biasing with positive electric field. A high degree of switching and backswitching is found for the film, the loop has become symmetric and nearly no voltage offset is detected.

The results of the measurement of the pyroelectric coefficient together with the C(V) curves show that the built in voltage offsets are strongly related to the pyroelectric coefficient. Possibly, the voltage offset poles the film during the cooling period of the sample after deposition. Voltage offsets in ferroelectric thin films are discussed in numerous papers [31–34]. In the model proposed by Warren et al. it is stated that voltage shifts arise from near interfacial trapping of electrons in the ferroelectric. On in situ pulsed laser deposition processed $La_{0.5}Sr_{0.5}CoO_3$ /PLZT $(Pb_{0.91}La_{0.09})$ $(Zr_{0.2}Ti_{0.8})$ $O_3/La_{0.5}Sr_{0.5}CoO_3$ films cooled under reducing (10^{-6} torr O_2) ambient large voltage offsets have been found. Films with the same composition and deposited at the same temperature of 650°C but cooled in 1 atm of oxygen after deposition exhibited very symmetric hysteresis loops. Shifts of the hysteresis loop by different combinations of UV illumination and application of bias voltages at 120°C together with the observed cooling atmosphere dependence leads to a model in which the voltage offsets are due to positively charged oxygen vacancies preferentially trapped near the bottom electrode and traps for electrons near each electrode. It was also found that the voltage shift reduces with increasing Zr content in the film [34].

Ferroelectric and pyroelectric properties of PZT thin films with different composition have also been investigated by Takayama et al. [30]. The films were deposited on Pt coated MgO single crystalline

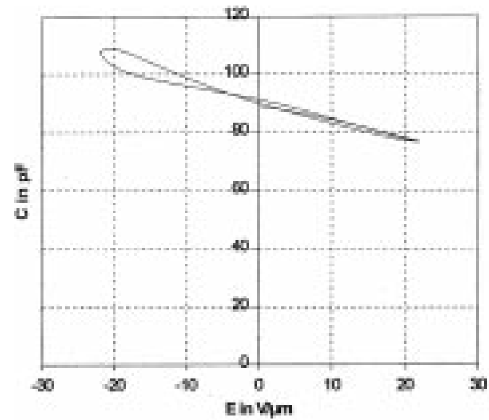

Fig. 13. C(V) curve of a self-polarized PZT(20/80) film.

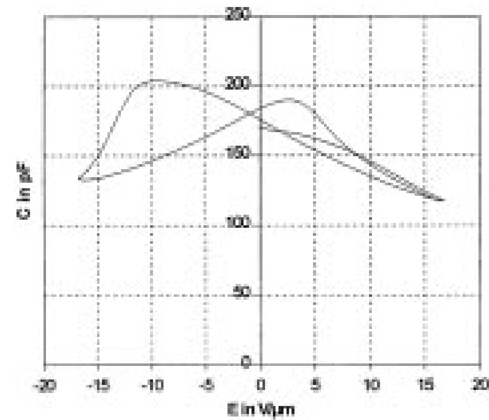

Fig. 14. C(V) curve of a PZT(38/62) film.

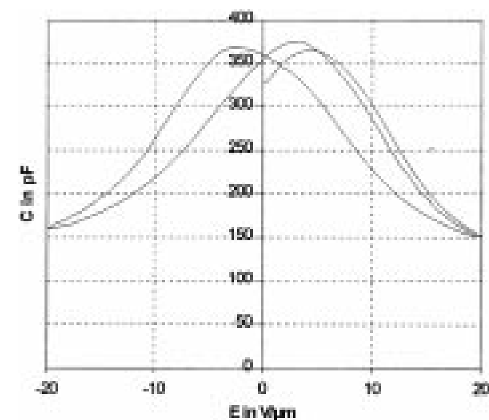

Fig. 15. C(V) curve of a PZT(60/40) film.

substrates. On that substrate the films grow with a high degree of c-axis orientation, i. e., in the films with tetragonal structure the polarization is directed vertical to the substrate surface resulting in optimum conditions for achieving high pyroelectric coefficients. Therefore, the values of up to 4×10^{-4} C/(m^2K) found for the pyroelectric coefficient are higher than the values presented in this paper for the [111] oriented films. On the rhombohedral side of the phase diagram the [111] direction is the polarization direction. As a consequence, the pyroelectric coefficient of the [001] oriented films described in [30] decreases. In the present paper the growth direction of the PZT is [111] and thus in a first order approximation one would expect an increase in the pyroelectric coefficient as now the polarization direction is perpendicular to the substrate surface. However, as shown in Fig. 12 the pyroelectric coefficient of the poled PZT(60/40) film is very much lower than the pyroelectric coefficient on the tetragonal side of the phase diagram. As mentioned earlier the films grow in the cubic phase during the deposition and undergo the phase transition during cooling. For the phase transition cubic to rhombohedral the cube expands along the [111] direction resulting in 8 crystallographic distinct variants, with the polarization along the <111> direction of the parent cubic phase. Only four of these are distinct deformation states and are given in Fig. 16. A detailed analysis is necessary to deduce possible domain configurations.

Such a detailed analysis has been performed for (001) oriented epitaxial rhombohedral films [35,36] and is not the scope of this paper for the [111] growth direction. However, as can be seen from Fig. 16 only for P_1^+ and P_1^- the polarization direction is perpendicular to the substrate surface. In all other cases P_2^+, P_3^+, P_4^+, P_2^-, P_3^- and P_4^- the polarization has an angle of about 109° or 71° to the [111] direction (71° and 109° domains). Thus a strong decrease in the pyroelectric coefficient can be expected for these orientations. Moreover, for these directions an elongation occurs parallel to the substrate surface. As was demonstrated by the stress temperature curves, Fig. 11, the PZT(60/40) film is under tensile stress at the phase transition thus preferring the P_2^+, P_3^+, P_4^+, P_2^-, P_3^- and P_4^- direction and together with the missing voltage shift this leads to an unpolarized film after cooling from the deposition temperature.

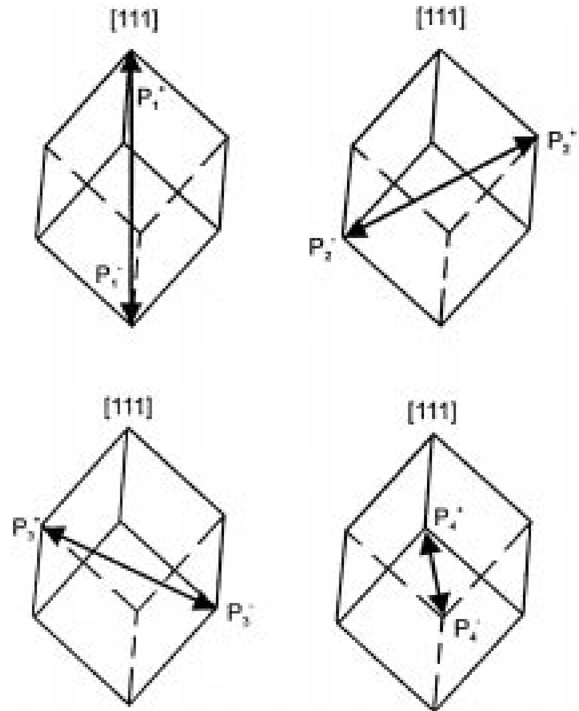

Fig. 16. Cell transformations and possible polarization directions for the cubic to rhombohedral transition of an [111] oriented film.

5. Summary and Conclusions

Planar multi target sputtering was used to deposit PZT films with a Zr content in the range of 0 to 60%. The stoichiometry of the films can simply be adjusted by the power to the different targets. Films with low Zr content are under compressive stress after deposition. Films with a Zr content up to about 25% exhibited favorable properties for the use in pyroelectric detector arrays. These films are self polarized, i.e., they exhibit pyroelectric coefficients of $> 2 \times 10^{-4}$ C/(m^2K) without poling, dielectric loss as low as 0.6% and high resistivity. High internal voltage offsets are found in these films which stabilize the polarization in the prepoled direction. The self polarization together with the high offset voltages fade out with increasing Zr content.

Future work will focus on doping of the ferroelectric films to further optimize the properties of the films for the use in thin film pyroelecric detector arrays.

Acknowledgments

We thank Barbara Jobst for many XRD traces taken on numerous samples and Dr. T. Kiendl for the analysis of the PZT films with EPMA.

References

1. R. Takayama, Y. Tomita, J. Asayama, K. Nomura, and H. Ogawa, *Sensors and Actuators*, **A21-A23**, 508 (1990).
2. D.L. Polla, C. Ye, and T. Tamagawa, *Appl. Phys. Lett.*, **59**, 3539 (1991).
3. M. Okuyama, K. Ohtani, T. Ueda, and Y. Hamakawa, *Int. J. Infrared and Millimeter Waves*, **6**, 71 (1985).
4. R. Bruchhaus, D. Pitzer, R. Primig, M. Schreiter, W. Wersing, N. Neumann, N. Hess, J. Vollheim, R. Köhler, and M. Simon, *Int. Ferroelectrics*, **17**, 369 (1997).
5. B.A. Tuttle, T.J. Garino, J.A. Voigt, T.J. Headley, D. Dimos, and M.O. Eatough, in *Science and Technology of Electroceramic Thin Films* (edited by O. Auciello and R. Waser), NATO ASI Series, **284**, (Dordrecht, 1995), pp. 117–132.
6. S.B. Desu, *J. Electrochem. Soc.*, **140**, 2981 (1993).
7. G.A.C.M. Spierings, G.J. Dormans, W.G.J. Moors, M.J.E. Ulenaers, and P.K. Larsen, *J. Appl. Phys.*, **78**, 1926 (1995).
8. G.A.C.M. Spierings, G.J. Dormans, W.G.J. Moors, M.J.E. Ulenaers, and P.K. Larsen, *Proc. ISAF '94* (eds. R. K. Pandey, M. Liu, and A. Safari), 29 (1995).
9. S.S. Sengupta, S.M. Park, D.A. Payne, and L.H. Allen, *J. Appl. Phys.*, **83**, 2291 (1998).
10. G.A.C.M. Spierings, J.M. Breed, M.J.E. Ulenaers, P.J. van Veldhoven, and P.K. Larsen, *Microelectronic Engineering*, **29**, 235 (1995).
11. J. Lappalainen, J. Frantti, and V. Lantto, *J. Appl. Phys.*, **82**, 3469 (1997).
12. R. Bruchhaus, D. Pitzer, R. Primig, W. Wersing, and Y. Xu, *Int. Ferroelectrics*, **14**, 141 (1997).
13. R. Bruchhaus, D. Pitzer, R. Primig, M. Schreiter, and W. Wersing, Int. Ferroelectrics, **21**, 461 (1998).
14. R. Bruchhaus, H. Huber, D. Pitzer, and W. Wersing, *Ferroelectrics*, **127**, 137 (1992).
15. B. Pachaly, R. Bruchhaus, D. Pitzer, H. Huber, W. Wersing, and F. Koch, *Integrated Ferroelectrics*, **5**, 333 (1994).
16. R. Bruchhaus, H. Huber, D. Pitzer, and W. Wersing, in *Proceedings of the Electroceramics IV*, edited by R. Waser (Aachen, 1994), 221.
17. T. Maeder, L. Sagalowicz, and P. Muralt, *Jpn. J. Appl. Phys.*, **37**, 2007 (1998).
18. D'Ans Lax, *Taschenbuch für Chemiker und Physiker*, Band 1, 3. Auflage, 1967, p. 1–148.
19. R. Stevens, ''Zirconia and Zirconia Ceramics'', *Magnesium Electron Publication No. 113*, 2nd edition, 1986.
20. S.R. Summerfelt, D. Kotecki, A. Kingon, and H.N. Al-Shareef, in *Ferroelectric Thin Films IV Materials Research Society Proc.*, **361**, 257 (1995).
21. J.M. Herbert, *Ceramic Dielectrics and Capacitors*, (New York, 1985), p. 171.
22. T. Maeder, P. Muralt, M. Kohli, A. Kholkin, and N. Setter, *Brit. Ceram. Proc.*, **54**, 207 (1995).
23. H. Adachi, T. Mitsuyu, O. Yamazaki, and K. Wasa, *Jpn. J. Appl. Phys.*, **24**, (Supplement 24-3), 13 (1985).
24. P. Muralt, T. Maeder, L. Sagalowicz, S. Hiboux, S. Scalese, D. Naumovic, R. G. Agostino, N. Xanthopouls, H.J. Mathieu, L. Patthey, and E.L. Bullock, *J. Appl. Phys.*, **83**, 3835 (1998).
25. R. Bruchhaus, H. Huber, D. Pitzer, and W. Wersing, *Integrated Ferroelectrics*, **2**, 157 (1992).
26. G.G. Stoney, *Proc. R. Soc. Fondon, Ser. A*, **82**, 182 (1909).
27. M. Klee, R. Eusemann, R. Waser, W. Brand, and H. van Hal, *J. Appl. Phys.*, **72**, 1566 (1992).
28. Y. Sakashita, T. Ono, H. Segawa, K. Tominaga, and M. Okada, *J. Appl. Phys.*, **69**, 8352 (1991).
29. K. Iijima, Y. Tomita, R. Takayama, and I. Ueda, *J. Appl. Phys.*, **60**, 361 (1986).
30. R. Takayama, Y. Tomita, K. Iijima, and I. Ueda, *Ferroelectrics*, **118**, 325 (1991).
31. D. Dimos, W. L. Warren, M. B. Sinclair, B. A. Tuttle, and R. W. Schwartz, *J. Appl. Phys.*, **76**, 4305 (1994).
32. G.E. Pike, W.L. Warren, D. Dimos, B.A. Tuttle, R. Ramesh, J. Lee, V.G. Keramidas, and J.T. Evans, Jr. *Appl. Phys. Lett.*, **66**, 484 (1995).
33. W.L. Warren, G.E. Pike, D. Dimos, K. Vanheusden, H.N. Al-Shareef, B.A. Tuttle, R. Ramesh, and J.T. Evans, Jr., in *Ferroelectric Thin Films V* edited by S. B. Deshu, R. Ramesh, B. A. Tuttle, R. E. Jones, In. K. Yoo, *Materials Research Soc. Proc.*, **433**, (Pittsburgh, 1996), p. 257.
34. W.L. Warren, B.A. Tuttle, D. Dimos, G.E. Pike, H.N. Al-Shareef, R. Ramesh, and J.T. Evans, Jr., *Jpn. J. Appl. Phys.*, **35**, 1521 (1996).
35. S.K. Streiffer, C.B. Parker, A.E. Romanov, M.J. Lefevre, L. Zhao, J.S. Speck, W. Pompe, C.M. Foster, and G.R. Bai, *J. Appl. Phys.*, **83**, 2742 (1998).
36. A.E. Romanov, M.J. Lefevre, J.S. Speck, W. Pompe, S.K. Streiffer, and C.M. Foster, *J. Appl. Phys.*, **83**, 2754 (1998).